Comparison of the structural properties of Zn-face and O-face single crystal homoepitaxial ZnO epilayers grown by RF-magnetron sputtering

R. Schifano, H. N. Riise, J. Z. Domagala, A. Yu. Azarov, R. Ratajczak, E. V. Monakhov, V. Venkatachalapathy, L. Vines, K. S. Chan, J. Wong-Leung, and B. G. Svensson

Citation: Journal of Applied Physics **121**, 015304 (2017); doi: 10.1063/1.4973342
View online: http://dx.doi.org/10.1063/1.4973342
View Table of Contents: http://aip.scitation.org/toc/jap/121/1
Published by the American Institute of Physics

Articles you may be interested in

Carrier localization in the vicinity of dislocations in InGaN
Journal of Applied Physics **121**, 013104 (2017); 10.1063/1.4973278

Extended defects in ZnO: Efficient sinks for point defects
Applied Physics Letters **110**, 022103 (2017); 10.1063/1.4973463

Optical and magnetic properties of Co-doped ZnO nanoparticles and the onset of ferromagnetic order
Journal of Applied Physics **121**, 013904 (2017); 10.1063/1.4973526

Investigation of the light-extraction efficiency in 280 nm AlGaN-based light-emitting diodes having a highly transparent p-AlGaN layer
Journal of Applied Physics **121**, 013105 (2017); 10.1063/1.4973493

DC voltage fields generated by RF plasmas and their influence on film growth morphology through static attraction to metal wetting layers: Beyond ion bombardment effects
Journal of Applied Physics **121**, 013301 (2017); 10.1063/1.4973483

Nanoscale visualization of electronic properties of $Al_xGa_{1-x}N/Al_yGa_{1-y}N$ multiple quantum-well heterostructure by spreading resistance microscopy
Journal of Applied Physics **121**, 014305 (2017); 10.1063/1.4973306

JOURNAL OF APPLIED PHYSICS **121**, 015304 (2017)

Comparison of the structural properties of Zn-face and O-face single crystal homoepitaxial ZnO epilayers grown by RF-magnetron sputtering

R. Schifano,[1,2,a)] H. N. Riise,[1] J. Z. Domagala,[2] A. Yu. Azarov,[1] R. Ratajczak,[3] E. V. Monakhov,[1] V. Venkatachalapathy,[1] L. Vines,[1] K. S. Chan,[4] J. Wong-Leung,[4] and B. G. Svensson[1]

[1]*Department of Physics/Center for Material Science and Nanotechnology, University of Oslo, P.O. Box 1048, Blindern, N-0316 Oslo, Norway*
[2]*Institute of Physics, Polish Academy of Sciences, Al. Lotników 32/46, 02-668 Warsaw, Poland*
[3]*National Centre for Nuclear Research, A. Soltana 7, 05-400 Otwock-Swierk, Poland*
[4]*Department of Electronic Materials Engineering, Research School of Physics and Engineering and Centre for Advanced Microscopy, The Australian National University, Canberra, Australian Capital Territory 2601, Australia*

(Received 16 September 2016; accepted 14 December 2016; published online 4 January 2017)

Homoepitaxial ZnO growth is demonstrated from conventional RF-sputtering at 400 °C on both Zn and O polar faces of hydrothermally grown ZnO substrates. A minimum yield for the Rutherford backscattering and channeling spectrum, χ_{min}, equal to ~3% and ~12% and a full width at half maximum of the 00.2 diffraction peak rocking curve of (70 ± 10) arc sec and (1400 ± 100) arc sec have been found for samples grown on the Zn and O face, respectively. The structural characteristics of the film deposited on the Zn face are comparable with those of epilayers grown by more complex techniques like molecular beam epitaxy. In contrast, the film simultaneously deposited on the O-face exhibits an inferior crystalline structure ~0.7% strained in the *c*-direction and a higher atomic number contrast compared with the substrate, as revealed by high angle annular dark field imaging measurements. These differences between the Zn- and O-face films are discussed in detail and associated with the different growth mechanisms prevailing on the two surfaces. *Published by AIP Publishing.* [http://dx.doi.org/10.1063/1.4973342]

I. INTRODUCTION

ZnO is a promising material for a wide variety of device applications ranging from optoelectronics to piezoelectricity and spintronics.[1–4] In this respect, the growth of films with device-worthy structural, optical, and electrical properties becomes crucial, and homoepitaxy represents a fascinating choice. In recent years, due to the commercial availability of high quality ZnO single crystal substrates, several studies on ZnO homoepitaxy have been published. However, up till now, among all the techniques investigated, the main focus has been on films deposited by plasma-assisted molecular beam epitaxy (*PA–MBE*),[5–7] metalorganic vapor-phase epitaxy (*MOVPE*),[8–10] chemical vapor deposition (*CVD*),[11] pulsed-laser deposition (*PLD*),[12,13] and atomic layer deposition (*ALD*);[14] for a review, see, for example, Ref. 15 and references therein. On the other hand, magnetron sputtering has been extensively investigated for obtaining polycrystalline transparent conductive oxide (*TCO*) films based on ZnO,[16] while less work has been devoted to sputtering based ZnO homoepitaxy.[17–20]

As an example, films with ~40 arc sec 00.2 rocking curve full width at half maximum (*FWHM*) have recently been obtained by Radio Frequency (*RF*) sputtering on pre-baked Zn face of hydrothermally grown (*HT*) ZnO wafers at a substrate temperature ≤500 °C.[18] Another study indicated that substrate temperatures of ~800 °C are necessary to obtain similar rocking curve *FWHM*s on films with comparable thickness.[19] Further, contradicting results on the surface polarity role have been reported suggesting a higher crystal quality, in terms of 00.2 rocking curve *FWHM*s, for depositions on the Zn-face,[19] the O-face,[20] or almost no polarity dependence.[17] Beside the structural characteristics of the films, their stoichiometry and structural defects are also key properties from a technological point of view; however, so far, little attention has been paid to these aspects.

In this study, it is shown that homoepitaxial single crystal stoichiometric ZnO films can be grown by *RF*-sputtering on the Zn face of *HT* ZnO wafers at 400 °C, using previously optimized deposition parameters for glass substrates.[21] Structural, crystallographic, and compositional analysis of the grown layers provide evidence of different optimum deposition conditions between O- and Zn-face, consistent with a polarity dependence of the growth mechanisms.

II. EXPERIMENTAL DETAILS

A commercially available 1 × 1 cm Tokyo Denpa *HT* wafer double sided polished and with a nominal resistivity equal to ~75 Ω cm was divided into two 1 × 0.5 cm pieces used for Zn and O face deposition and labeled hereafter as samples *A* and *B*, respectively. These two samples are part of a study based on a batch of 14 samples in total.[22] Afterwards, acetone, ethanol, and deionized water cleaning was performed for 5 min each sequentially, prior to loading them simultaneously into a Semicore Tri-axis Multi Source Sputtering

a)Electronic mail: schifano@ifpan.edu.pl

System balanced magnetron sputtering deposition system. As ZnO source, a 99.99% pure ZnO ceramic target mounted on a *RF*-powered 3 in. cathode was used, and the target to substrates distance was set equal to ~11 cm. The ZnO substrates were placed on a quartz support corresponding to a sample floating potential condition. The sample chamber was evacuated to a base pressure of $\sim 6 \times 10^{-7}$ Torr. After reaching the desired deposition substrate temperature of 400 °C, 99.999% pure Ar was introduced to a pressure of ~17 mTorr. The film deposition was performed by keeping the ZnO cathode power at 50 W and the rotation of the sample stage at 12 rpm. A pre-sputtering time of 10 min for cleaning the target was performed, and subsequently, the shutter was opened. The deposition lasted 5 h corresponding to an expected film thickness of (560 ± 30) nm on glass substrates according to a previous work.[21] The cathode voltage during deposition was constant at a level of (177 ± 1) V.

The sputtered thin films were analyzed by Rutherford backscattering spectrometry in channeling (*RBS/C*) and random mode (*RBS/R*) with 3.085 MeV $^4He^{++}$ ions incident along the [00.1] direction and a Si surface barrier based detector positioned at 165° relative to the incident beam direction. The energy of the incident $^4He^{++}$ ions was selected in order to exploit the O resonance[23,24] and accurately verify the stoichiometry of the films. A $1 \times 1\,mm^2$ beam size was used, the detector resolution was 15 keV and no bias was applied to the samples. The stoichiometry of the grown layers was determined by comparing the deposited layers *RBS/R* spectra with those of a single crystal ZnO wafer, anticipated to be stoichiometric. In addition, from the *RBS/C* and *RBS/R* measurements, the minimum yield, χ_{min} was extracted as well. Finally, the *RBS* spectra channel width was converted to Zn depth using the stopping power given by the SRIM code[25] and assuming the ZnO atomic density equal to $8.3 \times 10^{22}\,cm^{-3}$.

The structural quality of the samples was investigated with a Bruker AXS D8 Discover X-ray diffractometer (*XRD*) and a High Resolution Philips X'Pert Diffractometer (*HXRD*) by using the CuKα_1 line selected by a 2 and 4 bounce Ge(022) asymmetric monochromator placed on the primary beam side, respectively. The $2\Theta - \omega$ scans shown were acquired with a position sensitive detector (LynxEye) utilized in the 1D mode (virtual receiving slit size = 75 μm), while for the transverse ω-scan, a three bounce Ge(220) analyzer in the diffracted path was used. Further, in double axis geometry, the Philips X'Pert diffractometer utilized a 1/4° receiving slit placed in front of the detector to record reciprocal space maps (*RSM*). Line profiles were fitted with a Voigt function. The full width at half maximum ($FWHM_V$) of the Voigt functions given in Sec. III has been corrected for the instrumental broadening according to the procedure outlined in Ref. 26.

Transmission electron microscopy (*TEM*), high resolution transmission electron microscopy (*HR–TEM*), and scanning transmission electron microscopy (*STEM*) were carried out on a JEOL 2100F instrument equipped with a field emission gun and operated at a 200 kV acceleration voltage. Cross-sectional *TEM* samples were prepared by mechanically polishing the films into wedge samples having a ~5° angle using an Allied tripod polisher, followed by ~2 h of Ar ion beam milling at low temperature (−168 °C) using a Gatan 691 Precision Ion Polishing System (*PIPS*) operated at 3.5 keV.

Finally, the samples and substrates surface morphology was investigated by Atomic force microscopy (*AFM*) measurements performed with a Veeco D3100 microscope running in tapping mode. The root mean square (*RMS*) surface roughness was deduced by averaging four 2.00 × 2.00 μm *AFM* amplitude images taken at different positions of the samples surfaces.

III. EXPERIMENTAL RESULTS

A comparison of *RBS/R* spectra of samples *A* and *B* and of a single crystal ZnO wafer acquired in random geometry is shown in Fig. 1(a). The results confirm that samples *A* and *B* are stoichiometric within the experimental accuracy (±1 at. %). The stoichiometry of the epilayers was also confirmed by simulated curves to the experimental spectra using the SIMNRA code[27] (not shown) even though, this is only indicative because of the uncertainty of the non-Rutherford

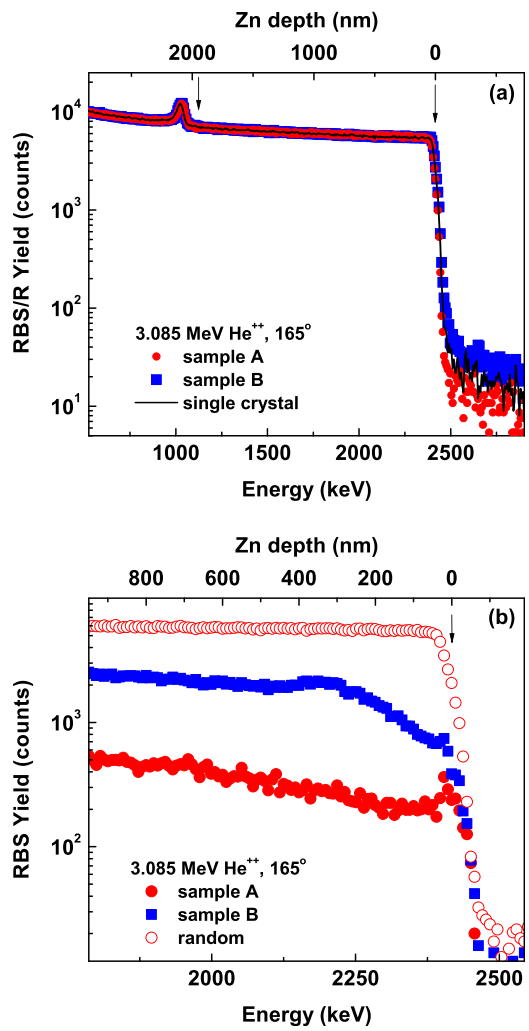

FIG. 1. (a) Comparison between the *RBS/R* spectra for samples *A*, *B* (scatter points) and a single crystal ZnO wafer (solid line). (b) *RBS/C* spectra for samples *A* and *B* and the *RBS/R* spectra of sample *A*. In both figures (a) and (b), the positions of the surface peaks of Zn and O are denoted by arrows.

TABLE I. χ_{min}, $FWHM_V$ of the 00.2 rocking curves fitted with a Voigt function, lattice parameters, lateral correlation length, $L_{\|}$, and angular tilt misorientation, α_{tilt}, for samples *A* and *B*. In the case of $L_{\|}$ and α_{tilt} the values in parentheses are the ones obtained by the single 00.2 transverse ω-scan profile analysis described in Ref. 37.

Sample	χ_{min}	c (Å)	a (Å)	$FWHM_V$ (arc sec)	$L_{\|}$ (μm)	α_{tilt} (arc sec)
A	~3	5.2074 ± 0.0001	3.2506 ± 0.0006	70 ± 10	~2.5	90 ± 10
					(3 ± 1)	(70 ± 10)
B	~12	5.243 ± 0.001	3.255 ± 0.007	1400 ± 100	0.12 ± 0.03	1300 ± 100
					(0.11 ± 0.04)	(1300 ± 100)

stopping power cross section. According to secondary ion mass spectrometry results, the H content is estimated to be $\sim 10^{20}\,cm^{-3}$ in the films with other unintentionally introduced impurities like Mg, Cl, Al, and Si occurring in the $\sim 10^{17}$–$10^{19}\,cm^{-3}$ range.[28] The *RBS/C* results for the *A* and *B* samples are shown in Fig. 1(b), together with the *RBS/R* of sample *A*. The extracted χ_{min} equals ~3% and ~12% for samples *A* and *B*, respectively, as summarized in Table I. The former value is similar to that (~2%–3%) typically recorded for single crystal *HT* ZnO wafers purchased from the same vendor.[29] Hence, the *RBS/C* measurements are suggesting a film crystalline quality of sample *A* comparable to that of the substrate, while for sample *B*, the higher χ_{min} and larger dechanneling vs Zn depth indicate a more defective epilayer. In addition, Fig. 1(b) reveals no bulk to film interface change in the slope of the *RBS/C* spectra for sample *A*, but for sample *B*, it occurs at a Zn depth of ~400 nm. Here, also the small peak in the yield may suggest a defective film-substrate interface. This indicates that the film deposited on the O-face is ~160 nm thinner than expected using glass substrates. This difference will be discussed in detail in Sec. IV. In Fig. 2, $2\theta - \omega$ scans of the 00.2 reflection are shown, and for sample *A*, the film related peak overlaps closely with the substrate one implying equal lattice constants in the *c*-direction. In contrast, for *B*, a distinct film peak is observed ~0.25° below the substrate signal, thus indicating a unit cell elongated in the *c*-direction. In Fig. 3(a), results from transverse ω-scans corresponding to the 00.2, 00.4, and 00.6 peak positions are shown for sample *A*. A $FWHM_V$ of the Voigt function describing the 00.2 transverse ω-scan, after eliminating the instrumental broadening, is extracted and found equal to (70 ± 10) arc sec. This is to be compared with a starting Zn- as well as O-face $FWHM_V$ within (20 ± 10) arc sec as measured on a substrate of the same batch and in agreement with what was previously reported by the vendor.[30] The value found for sample *A* here is similar to that previously obtained by *RF*-sputtering on substrates kept at ~800 °C and comparable to the values recently reported for films obtained by *MOVPE*, *PLD*, and *PA–MBE*, typically in the ~20–40 arc sec range.[10,19,31] The peak widths in the transverse ω-scans are much broader for sample *B*, as can be seen in Fig. 3(b), and indicating a poor crystal quality of the grown epilayer. This is consistent with the *RBS/C* results. In addition, a close look on

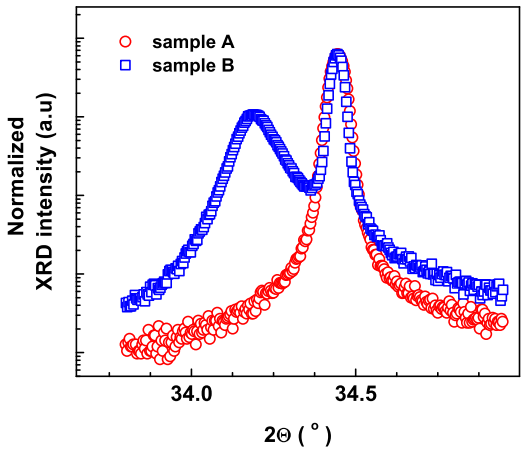

FIG. 2. 00.2 reflection $2\theta - \omega$ scans for samples *A* and *B* normalized to the main/substrate peak intensity.

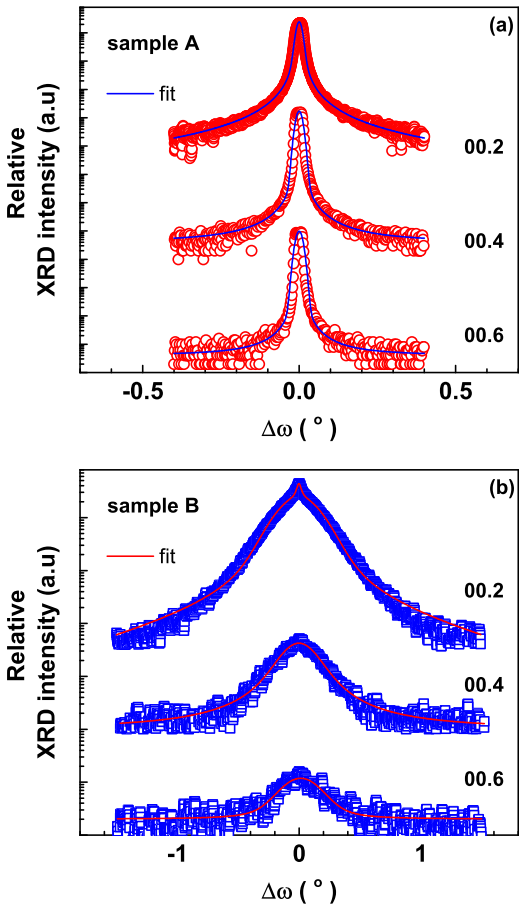

FIG. 3. 00.2, 00.4, and 00.6 transverse ω-scans for samples *A* and *B* in (a) and (b), respectively. In both cases, the curves are displaced along the intensity axis for clarity, and the Voigt functions used to model the experimental data are indicated by solid lines (two Voigt functions centered in $\Delta\omega$ equal to 0 have been used to fit the 00.2 peak in the case of sample *B*). Note that the large maximum and dynamical intensity difference between samples *A* and *B* is related not only to the superior crystal quality of the former, but also to the presence of an overlapping substrate contribution.

the 00.2 data in Fig. 3(b) actually reveals the existence of two contributions: a broad diffuse component and a sharper one with a $FWHM_V$ of (1400 ± 100) arc sec and (150 ± 40) arc sec, respectively. Furthermore, at the higher orders of reflection, the sharp component vanishes. The presence of two components in the 00.2 transverse ω-scan can be related to: (i) a substrate surface related streak overlapping with the film signal,[32] (ii) an unconventional mosaic structure of the film with the single crystallites coherently scattering the X-rays because of a long range order due to the substrate film interfacial interactions.[33] In the latter case, the specular component is attenuating at high reflection orders due to the residual disorder present, whereas in the former case, it disappears due to the increasing angular distance between the substrate/film peak positions. Both interpretations are consistent with the results obtained, and further measurements are necessary to distinguish between the two physical mechanisms. Here, it is also worth pointing out that rocking curves showing similar characteristics have also been reported for ZnO films grown by *PA–MBE* on *c*-sapphire substrate.[34] In this case, interfacial degradation due to the large lattice mismatch to the substrate was discussed as a possible reason for the double peak feature. However, in our case, the absence of a double peak for the high order reflections excludes the occurrence of a two region structure along the growth direction, as expected, since no lattice mismatch is present. In the following, the broad diffuse component $FWHM_V$ is taken as a figure of merit of the crystallographic quality of sample *B* and used to extract relevant film characteristics.

For transverse ω-scans corresponding to symmetric reflections, the averaged lateral correlation length, $L_{\parallel}$, is independent on the scattering vector, **Q**. On the other hand, the angular tilt misorientation, α_{tilt}, causes a broadening (in arcs) in the reciprocal space and is therefore proportional to **Q**. Hence, a Williamson–Hall like plot[35] can be utilized to separate $L_{\parallel}$ and α_{tilt}. By considering the relations linking the angular space coordinates to the reciprocal space ones, a Williamson–Hall like plot will, in this case, become: $\beta \times (\sin\theta)/\lambda$ vs. $\sin\theta/\lambda$, where β is the transverse ω-scan integral breath expressed in rad, θ the corresponding Bragg angle, and λ the CuKα_1 wavelength. Then, α_{tilt} corresponds to the slope of the linear dependence, while $L_{\parallel}$ can be extracted from the intercept with the ordinate, y_0, according to the relation $L_{\parallel} = 1/2y_0$.[36] The resulting Williamson–Hall like plots for samples *A* and *B*, obtained by using the β of the Voigt function modeling the ω-scan presented in Fig. 3, are shown in Fig. 4. As given in Table I, $L_{\parallel}$ and α_{tilt} are found equal to ~2.5 μm and (90 ± 10) arc sec for sample *A* and to (120 ± 30) nm and (1300 ± 100) arc sec for sample *B*. In order to substantiate these values, which suffer from a low signal to noise ratio for the high-order reflections of sample *B*, also a single 00.2 transverse ω-scan profile analysis has been performed.[37] According to this analysis, the Voigt function is related to $L_{\parallel}$ and α_{tilt} via the Lorentzian and Gaussian component of the peak, respectively, assuming a random distribution of mosaic blocks around the growth direction.[37] A fairly good agreement between the two methods is found for both samples, as illustrated in Table I. The values of α_{tilt} for sample *A* are comparable to those reported (~20 arc sec) for ZnO layers grown on *c*-sapphire by

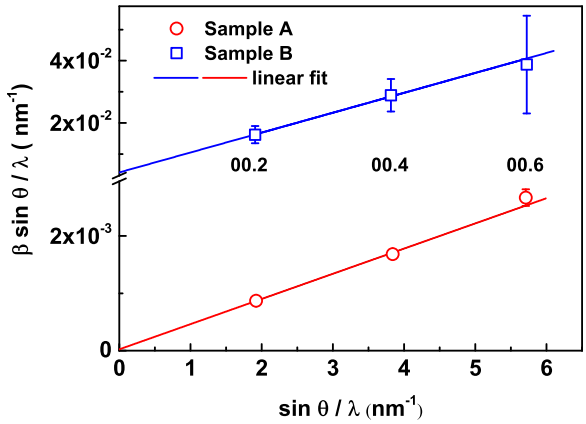

FIG. 4. (a) Graphical separation of the contributions from the lateral correlation length, $L_{\parallel}$, and the angular tilt misorientation, α_{tilt}, to the broadening of the transverse ω-scans integral breath, β, based on a Williamson–Hall like plot.

PA–MBE utilizing a MgO/ZnO buffer bilayer followed by annealing at 750 °C prior to the ZnO film deposition.[34] Similarly, also the large $L_{\parallel} \sim 3$ μm confirms the good crystallographic property of sample *A*. On the other hand, for sample *B*, both α_{tilt} and $L_{\parallel}$ are in the range of the values generally reported for heteroepitaxially grown ZnO layers.[34,38,39]

The *RSM* results of the asymmetrical −10.5 reflection are shown in Figs. 5(a) and 5(b). For sample *B*, the film node is clearly separated from the substrate peak and occurs at smaller Q_y. The elliptic shape of the ZnO node is elongated along the Q_x axis, indicating that the dominant broadening is due to the limited lateral correlation length, $L_{\parallel}$.[40] In contrast, no distinct epilayer peak occurs for sample *A*, see Fig. 5(b), consistent with the symmetrical reflection shown in Fig. 2. Furthermore, a factor of ~3 reduction both in the $\mathbf{Q_x}$ and $\mathbf{Q_y}$ extension of the signal tails is observed, corroborating the overall better crystal quality of sample *A* relative to sample *B*. From the −10.5 asymmetrical scans shown in Fig. 5 and the $2\theta - \omega$ scans 00.6 peak position (not shown), the lattice constants *a* and *c* have been evaluated and are listed in Table I. Corrections for refraction effects due to the difference in refractive index between the sample and air, have been omitted in these calculations.[32] Here, it is interesting to notice that the *a* lattice constant is identical for the two samples within the experimental errors, while for sample *B*, the *c* lattice constant is found ~0.7% elongated with respect to the substrate/sample *A*, as already discussed.

Figs. 6(a) and 6(b) show selected area diffraction patterns (*SAED*) of the samples *A* and *B*, respectively. A sharply defined spot pattern is observed for both samples consistent with single crystalline homoepitaxial layers. *HR–TEM* images of the substrate-film interface taken along the *a*-axis reveal a more defective interface in sample *B* (Fig. 4(d)) compared to sample *A* (Fig. 4(c)). In addition, the presence of threading dislocations originating from the substrate-film interface and reaching the surface has been revealed by two-beam bright field imaging close to the *m*-axis in sample *A*, as shown in Fig. 6(e). Diffraction contrast analysis suggest that the Burgers vector, **b**, of these defects are of edge-type and parallel to the {11.0} directions. The presence of these

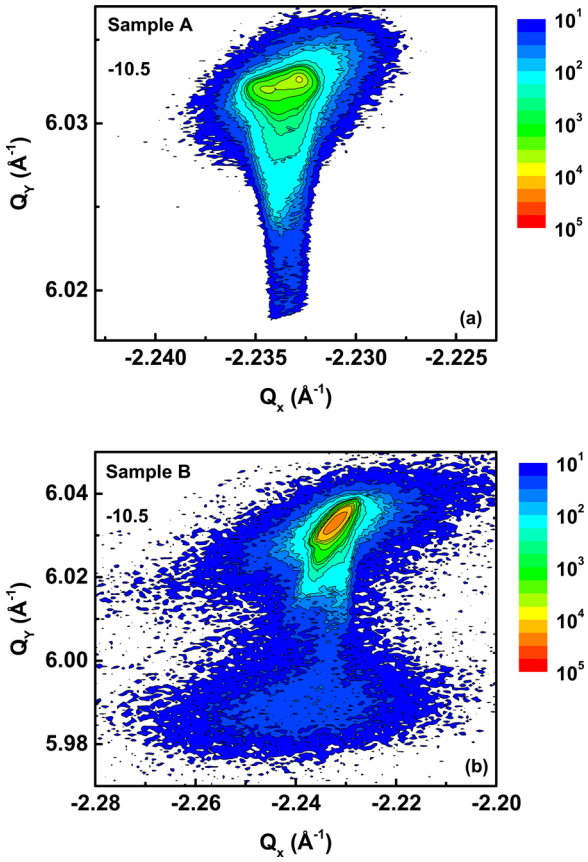

FIG. 5. Reciprocal scan maps, *RSM*, relative to the −10.5 reflection for sample *A* and *B*. Note that the scale for sample *B* is a factor 4 larger in each direction than that of sample *A*, while the absolute differences in intensity involve the use of a two bounce hybrid Ge(220) monochromator and a double axis geometry with a 1/4° receiving slit placed in front of the detector for samples *A* and *B*, respectively.

dislocations confirms that the film is a relaxed single crystal layer and they have been reported as the most abundant type of threading dislocations in *PA–MBE* grown ZnO films deposited on *c*-sapphire with and without a MgO buffer layer.[34] It is important to note that such pure edge dislocations will affect only (*hk.l*) planes with at least *h* or *k* nonzero, i.e., the $FWHM_V$ of the transverse ω-scans corresponding to symmetric reflections in Fig. 3(a) will not be influenced and hence not reveal the presence of the pure edge dislocations. A similar analysis of sample *B* did neither unveil any distinct dislocations, see, for example, Fig. 6(f) where the *TEM* image along the *a*-axis is shown, nor evidence for other extended defects, like basal stacking faults. Note also that a comparison between these two cross sectional two-beam bright field images (Figs. 6(e) and 6(f)) reveals a substantial difference in thickness between the epilayers grown on the Zn face (sample $A \sim 800$ nm) and the O face (sample $B \sim 400$ nm). This occurs despite that the two layers were prepared simultaneously and is far beyond the ∼5% thickness fluctuations observed for previous polycrystalline films.[21] Furthermore, in both cases, the film thicknesses deviate significantly from the expected one of ∼560 nm, based on films deposited on glass substrates using the same growth conditions.[21]

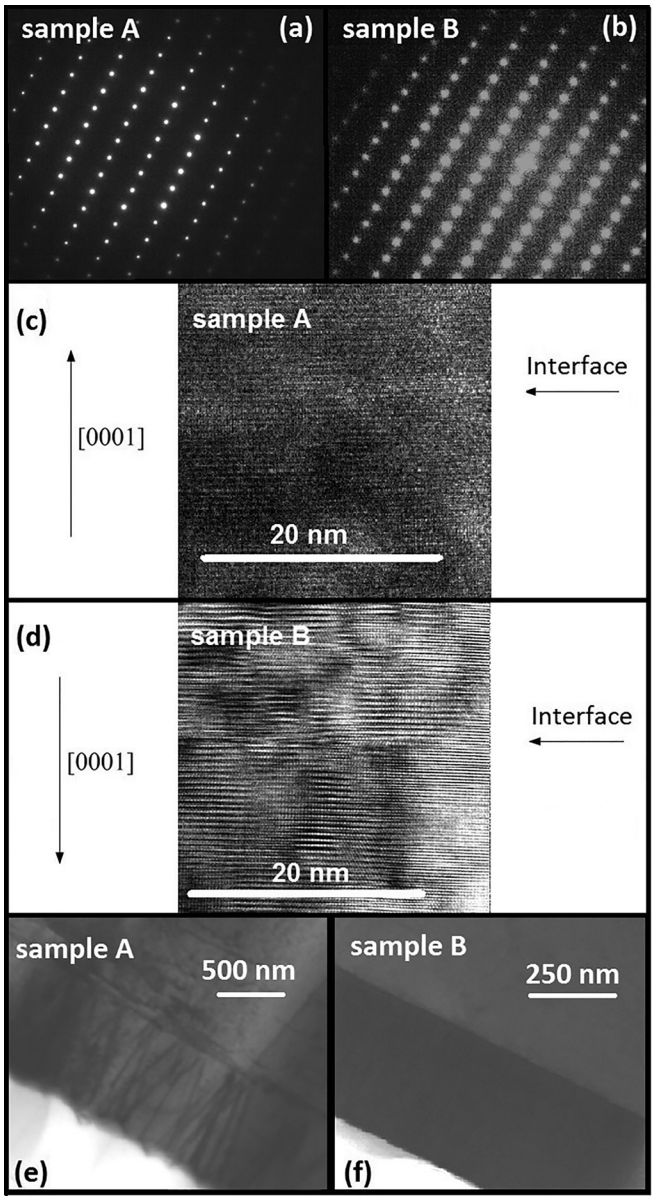

FIG. 6. (a) and (b) *SAED* patterns from the as-deposited films. (c)–(f) *HR–TEM* and *TEM* images of the interfacial region and of the overall film. (a), (c), (e) and (b), (d), (f) correspond to samples *A* and *B*, respectively. All the images shown were taken along the *a*-axis.

Comparison of the *TEM* cross section images of the films with those of the substrates reveals that sample *B* exhibits a darker contrast than the bulk (see Fig. 6(f)). Further investigations based on *STEM* analysis using high angle annular dark field (*HAADF–STEM*) imaging reveal a higher atomic number (*Z*) contrast with respect to the substrate, Fig. 7. This indicates a slightly Zn rich and/or denser layer, leading to the darker appearance in the *TEM* cross section image (Fig. 6(f)). Comparison with the *RBS/R* results suggests that in the former case the Zn excess has to be within the measurement accuracy of ≲1 at. %. In addition, a close look to the sample *B* cross section *HAADF–STEM* images reveal subtle contrasts variations. This may point to non-homogeneity in the composition and/or to slightly denser areas due to strain within the layer as well as close to the substrate interface. However, no evidence for the

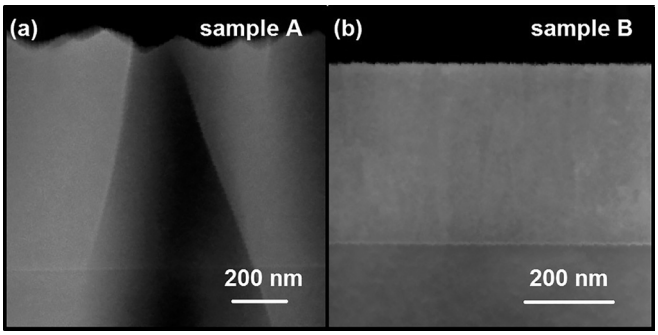

FIG. 7. (a) and (b) Cross section *HAADF–STEM* images for samples *A* and *B*, respectively.

presence of Zn precipitates has been found. On the other hand, no significant *Z*-contrast difference is observed between the substrate and the epitaxial layer of sample *A*. This is in agreement with the superior quality of sample *A* with structural characteristics closer to those of the substrate, as presented above. On the contrary, Zn excess has been previously reported as substantially affecting the structural properties of ZnO single crystal epitaxial films[41] consistently with the poorer crystal quality of sample B observed here.

AFM measurements in tapping mode were performed on both the *A* and *B* samples prior and after the deposition. The surface of the bare wafer (not shown) appears to be atomically flat with no clear step and terrace structure and a root mean square (*RMS*) roughness equal to (0.3 ± 0.1) nm and (0.2 ± 0.1) nm for the Zn- and O-face, respectively, in agreement with what previously reported by the vendor.[30] On the contrary, the morphology of the deposited films result strikingly different, thus suggesting a growth mechanism diverse on the Zn- and O-face as shown in Fig. 8, where two typical surface images are displayed. For sample *A*, large elongated grains of micrometer size with the presence of submicrometer features are clearly visible and a *RMS* surface roughness equal to (12.2 ± 0.6) nm is obtained. For sample *B*, a smoother surface with a uniform distribution of more circular grains with diameter of $\sim$100 nm and (1.0 ± 0.1) nm *RMS* surface roughness is observed. For both samples, the grain sizes measured by *AFM* are in fairly good agreement with the values of $L_{\|}$ extracted from the *XRD* measurements, indicating that the surface morphology correlates with the underlying mosaic structure of the films.

IV. DISCUSSION

The results evidence striking differences in the crystal quality, crystallographic defects present, surface morphology, and even epilayer thickness depending on the surface polarity of the ZnO wafer used as a substrate.

Concerning the $\sim$400 nm thickness difference observed between samples *A* and *B*, epitaxial ZnO growth has been reported to depend significantly on the surface polarity in the case of *PA–MBE* depositions.[6] In fact, the observed difference in thickness follows the trend expected: on the O polar surface, Zn species are incorporated at the step edges, while on the Zn polar one, the Zn atoms are incorporated directly on the surface due to the three-bond configuration of the

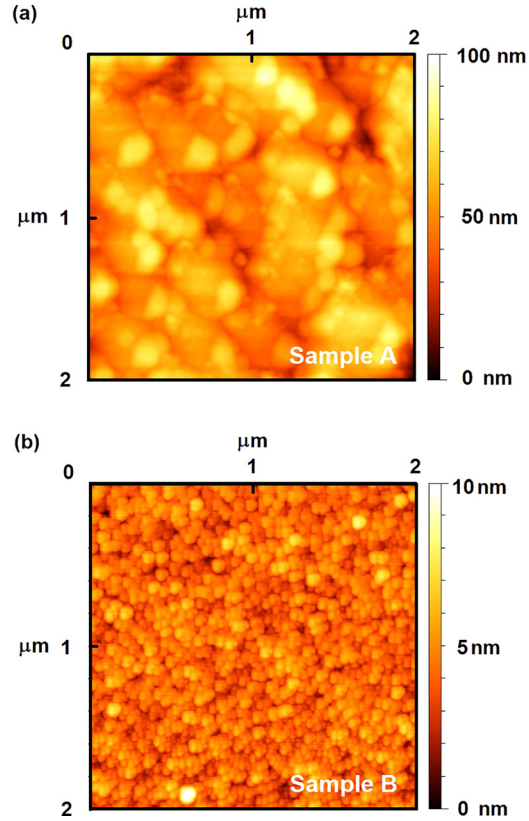

FIG. 8. (a) and (b) Tapping mode *AFM* images for samples *A* and *B*, respectively. The *z*-scale is given on the right hand side of the respective figure, and for sample *B*, it is 10 times smaller than for sample *A*.

underlying O-layer. This results in a higher growth rate in the latter case and for amorphous substrates, like glass, yielding randomly oriented grains, an intermediate growth rate is anticipated.[42] Hence, the deviations from a polycrystalline ZnO film growth rate are fully consistent with an epitaxial growth regime, where a one to one correlation between the mass transfer and deposition rate does not apply. A high homoepitaxial deposition rate has also been observed in the related study where the *RF*-magnetron sputtered ZnO films, deposited on the Zn-face of ZnO single crystals, were compared with polycrystalline ones grown simultaneously on Si (100) *RCA* cleaned substrates.[22]

In addition, the 3-dimensional growth observed for sample *A* (Zn face) by *AFM* suggests a too high Zn/O ratio, considering the low Zn mobility due to the three-bond configuration of the underlying O-layer.[6] In the case of O-face because of the step edges incorporation of the Zn species, the growth will be less affected by the Zn/O ratio. However, a reduction in island size from $\sim$3 μm to $\sim$200 nm with the Zn/O ratio increasing from 0.2 to 2 has been reported in Ref. 6. This finding is in qualitative agreement with the submicrometer features observed here in Fig. 8(b) for sample *B*. Hence, using an optimal mixture of Ar and O as "working" gas is anticipated to further improve the film structural characteristics.

Sample *A* is found exhibiting a fully relaxed structure with edge-type threading dislocations parallel to the {11.0} directions. On the contrary, sample *B* is found to be $\sim$0.7% elongated in the *c*-direction, while there is in plane matching

between the substrate and epilayer. This indicates that the film is not purely biaxially strained as generally found for polycrystalline magnetron sputtered ZnO films deposited on amorphous substrates[43] and it is specular to what was reported, for example, in the case of *PLD* grown ZnO on AlN.[44] Moreover, the *HAADF–STEM* imaging suggests that sample *B* is slightly Zn rich within the *RBS/R* accuracy of $\lesssim$1 at. % and/or denser. Since no evidence of extended defects is revealed by *TEM*, these results suggest a distribution of small size defects like single or clusters of point defects. They are presumably Zn related and anticipated to introduce hydrostatic strain,[45] contributing to the extension of the lattice in the *c*-direction. Here, it is worth noticing that similar *c*-lattice constant extension for *DC*- and *RF*-sputtered polycrystalline ZnO:Al films has been reported.[46] It was ascribed to O^- ions (with energy in the 60−450 eV range) being implanted into the growing ZnO film with a subsequent formation of acceptor-like oxygen interstitials. The surface polarity is, however, expected to have minor effect on the amount of atoms, ions, or molecules peening/implanted and in our case they are excluded as main reason for the striking differences between samples *A* and *B*.

Because of the lower growth rate (longer exposure time), the O-face is anticipated to be more affected by re-sputtering as well as surface atomic displacements produced by the bombarding ions. Therefore, during O-face depositions, a higher density of surface defects occurs, and they may play a major role being nucleation sites for the incorporation of excess Zn atoms at step edges. Hence, the growth process in itself may be enhancing the evolution of a more defective (strained) and/or denser as well as Zn rich epilayer on the O-face. Here, it is important to underline that the Zn rich structure of sample *B* cannot be attributed to the Zn rich growth conditions since the growth on the O face is almost independent on the Zn/O ratio, as discussed above. Moreover, in addition to a higher density of generated defects on the O-face, the nature of the defects is also likely to differ from that on the Zn-face.[47,48] This will, indeed, affect the epitaxial growth mechanisms on the two faces. Further investigations with variable Ar gas pressure during the sputtering process should be pursued to elucidate the importance of the different physical mechanisms involved.

V. CONCLUSIONS

In conclusion, single crystal homoepitaxial ZnO layers were grown at 400 °C by conventional RF-sputtering on both Zn and O polar faces of commercially available hydrothermally grown substrates. A $FWHM_V$ of the 00.2 transverse ω-scan (modeled as a Voigt function) as low as (70 ± 10) arc sec was obtained for the Zn face film. These results together with a smooth epi-layer/bulk interface show that RF-magnetron sputtering is a viable alternative to more complex techniques like *PA–MBE* or *MOCVD* to grow epitaxial ZnO films of device-worthy quality on the Zn face. In contrast, a much broader $FWHM_V$ of the 00.2 transverse ω-scan equal to (1400 ± 100) arc sec for the layer deposited on the O-face has been measured with *HAADF–STEM* revealing a Zn rich and/or denser film. Further, the Zn-face film is relaxed exhibiting threading dislocations, while the O-face film is highly strained. These results imply two different optimal windows for the O and Zn-face homoepitaxial growth of ZnO films by *RF*-magnetron sputtering, linked to the polarity dependence of the growth mechanism.

Finally, the present study shows the prospective for RF-magnetron sputtered homoepitaxially grown ZnO layers of even higher crystallographic quality by further fine tuning of the deposition conditions.

ACKNOWLEDGMENTS

This work has been performed within "The Norwegian Research Centre for Solar Cell Technology" Project No. 193829, a Centre for Environment-friendly Energy Research co-sponsored by the Norwegian Research Council and research and industry partners in Norway and the Frienergi program. R.S. acknowledges the partial support from the EU 7th Framework Programme Project No. REGPOT-CT-2013-316014 (EAgLE).

[1] C. F. Klingshirn, B. K. Meyer, A. Waag, A. Hoffmann, and J. Geurts, *Zinc Oxide From Fundamental Properties Towards Novel Applications* (Springer-Verlag, Berlin Heidelberg, 2010).
[2] C. Jagadish and S. J. Pearton, *Zinc Oxide Bulk, Thin Films and Nanostructures* (Elsevier, Oxford, 2006).
[3] S. Ramachandran, A. Tiwari, and J. Narayan, Appl. Phys. Lett. **84**, 5255 (2004).
[4] A. Tiwari, C. Jin, A. Kvit, D. Kumar, J. Muth, and J. Narayan, Solid State Commun. **121**, 371 (2002).
[5] K. Sakurai, M. Kanehiro, K. Nakahara, T. Tanabe, S. Fujita, and S. Fujita, J. Cryst. Growth **209**, 522 (2000).
[6] H. Kato, M. Sano, K. Miyamoto, and T. Yao, J. Cryst. Growth **265**, 375 (2004).
[7] H. Xu, K. Ohtani, M. Yamao, and H. Ohno, Appl. Phys. Lett. **89**, 071918 (2006).
[8] T. P. Smith, H. McLean, D. J. Smith, and R. F. Davis, J. Cryst. Growth **265**, 390 (2004).
[9] S. Heinze, A. Krtschil, J. Bläsing, T. Hempel, P. Veit, A. Dadgar, J. Christen, and A. Krost, J. Cryst. Growth **308**, 170 (2007).
[10] T. Ive, T. Ben-Yaacov, C. G. V. de Walle, U. K. Mishra, S. P. Denbaars, and J. S. Speck, Phys. Status Solidi C **6**, 1460 (2009).
[11] C. Neumann, S. Lautenschläger, S. Graubner, J. Sann, N. Volbers, B. K. Meyer, J. Bläsing, A. Krost, F. Bertram, and J. Christen, Phys. Status Solidi B **244**, 1451 (2007).
[12] D. J. Rogers, F. H. Teherani, A. Largeteau, G. Demazeau, C. Moisson, D. Turover, J. Nause, G. Garry, R. Kling, T. Gruber, A. Waag, F. Jomard, P. Galtier, A. Lusson, T. Monteiro, M. J. Soares, A. Neves, M. C. Carmo, M. Peres, G. Leronde, and C. Hubert, Appl. Phys. A **88**, 49 (2007).
[13] H. von Wenckstern, H. Schmidt, C. Hanisch, M. Brandt, C. Czekalla, G. Benndorf, G. Biehne, A. Rahm, H. Hochmuth, M. Lorenz, and M. Grundmann, Phys. Status Solidi RRL **1**, 129 (2007).
[14] L. Wachnicki, A. Duzynska, J. Z. Domagala, B. S. Witkowski, T. A. Krajewski, E. Przezdziecka, M. Guziewicz, A. Wierzbicka, K. Kopalko, S. Figge, D. Hommel, M. Godlewski, and E. Guziewicz, Acta Phys. Pol. A **120**, A7 (2011).
[15] H. Morkoç and Ü. Özgür, *Zinc Oxide: Fundamentals, Materials and Device Technology* (Wiley-VCH Verlag GmbH & Co., Weinheim, 2009).
[16] K. Ellmer, A. Klein, and B. Rech, *Transparent Conductive Zinc Oxide* (Springer-Verlag, Berlin, Heidelberg, 2008).
[17] S. Eisermann, J. Sann, A. Polity, and B. K. Meyer, Thin Solid Films **517**, 5805 (2009).
[18] A. Bikowski and K. Ellmer, J. Appl. Phys. **114**, 063709 (2013).
[19] I. Kim, S. Jeong, and B. Lee, Semicond. Sci. Technol. **22**, 683 (2007).
[20] S. Zhu, C.-H. Su, S. L. Lehoczky, M. T. Harris, M. J. Callahan, P. McCarty, and M. A. George, J. Cryst. Growth **219**, 361 (2000).
[21] R. Schifano, M. Schofield, L. Vines, S. Diplas, E. V. Monakhov, and B. G. Svensson, IOP Conf. Ser.: Mater. Sci. Eng. **34**, 012007 (2012).

[22]H. N. Riise, V. S. Olsen, A. Y. Azarov, A. Galeckas, T. N. Sky, B. G. Svensson, and E. V. Monakhov, Thin Solid Films **601**, 18 (2016).
[23]J. A. Leavitt, L. C. McIntyre, M. D. Ashbaugh, J. G. Oder, Z. Lin, and B. Dezfouly-Arjomandy, Nucl. Instrum. Methods Phys. Res., Sect. B **44**, 260 (1990).
[24]A. Y. Azarov, A. Hallén, B. Svensson, X. Du, and A. Y. Kuznetsov, Nucl. Instrum. Methods B **272**, 426 (2012).
[25]See http://www.srim.org/ for details on the SRIM code.
[26]T. H. D. Keijser, J. I. Langford, E. J. Mittemeijer, and A. B. P. Vogels, J. Appl. Cryst. **15**, 308 (1982).
[27]See http://home.mpcdf.mpg.de/~mam/index.html for details on the SIMRA code.
[28]L. Vines, R. Schifano, M. Schofield, and B. G. Svensson, Phys. Scr. T **2012**, 014005.
[29]A. Y. Azarov, A. Hallen, X. Du, P. Rauwel, A. Kuznetsov, and B. Svensson, J. Appl. Phys **115**, 073512 (2014).
[30]K. Maeda, M. Sato, I. Niikura, and T. Fukuda, Semicond. Sci. Technol. **20**, S49 (2005).
[31]M. Lorenz, G. Wagner, A. Rahm, H. Schmidt, H. Hochmuth, H. Schmid, W. Mader, M. Brandt, H. von Wenckstern, and M. Grundmann, Phys. Status Solidi C **5**, 3280 (2008).
[32]M. A. Moram and M. E. Vickers, Rep. Prog. Phys. **72**, 036502 (2009).
[33]P. F. Miceli and C. J. Palmstrøm, Phys. Rev. B **51**, 5506 (1995).
[34]M. W. Cho, A. Setiawan, H. J. Ko, S. K. Hong, and T. Yao, Semicond. Sci. Technol. **20**, S13 (2005).
[35]M. Birkholz, *Thin Films Analysis by X-Ray Scattering* (Wiley-VCH Verlag GmbH & Co., Weinheim, 2006).
[36]T. Metzger, R. Höpler, E. Born, O. Ambacher, M. Stutzmann, R. Stömmer, M. Schuster, H. Göbel, S. Christiansen, M. Albrecht, and H. P. Strunk, Philos. Mag. A **77**, 1013 (1998).
[37]T. H. D. Keijser, E. J. Mittemeijer, and H. C. F. Rozendaal, J. Appl. Cryst. **16**, 309 (1983).
[38]O. Durand, A. Letoublon, D. J. Rogers, and F. H. Teherani, Thin Solid Films **519**, 6369 (2011).
[39]M. Guziewicz, R. Schifano, E. Przezdziecka, J. Z. Domagala, W. Jung, T. A. Krajewski, and E. Guziewicz, Appl. Phys. Lett. **107**, 101105 (2015).
[40]R. Chierchia, T. Böttcher, H. Heinke, S. Einfeldt, S. Figge, and D. Hommel, J. Appl. Phys. **93**, 8918 (2003).
[41]J. F. Muth, R. M. Kolbas, A. K. Sharma, S. Oktyabrsky, and J. Narayan, J. Appl. Phys. **85**, 7884 (1999).
[42]W. Zhang, Ph.D. thesis, Forschungszentrum Jülich GmbH, 2012.
[43]R. Cebulla, R. Wendt, and K. Ellmer, J. Appl. Phys. **83**, 1087 (1998).
[44]C. Jin, R. Narayan, A. Tiwari, H. Zhou, A. Kvit, and J. Narayan, Mater. Sci. B **117**, 348 (2005).
[45]C. Kisielowski, J. Krüger, S. Ruvimov, T. Suski, J. W. Ager III, E. Jones, Z. Liliental-Weber, M. Rubin, E. R. Weber, M. D. Bremser, and R. F. Davis, Phys. Rev. B **54**, 17745 (1996).
[46]A. Bikowski, T. Welzel, and K. Ellmer, Appl. Phys. Lett. **102**, 242106 (2013).
[47]T. Ohnishi, A. Ohtomo, M. Kawasaki, K. Takahashi, M. Yoshimoto, and H. Koinuma, Appl. Phys. Lett. **72**, 824 (1998).
[48]M. W. Allen, D. Y. Zemlyanov, G. I. N. Waterhouse, J. B. Metson, T. D. Veal, C. F. McConville, and S. M. Durbin, Appl. Phys. Lett. **98**, 101906 (2011).